

Spatial mapping of band bending in semiconductor devices using in situ quantum sensors

D. A. Broadway^{1,2,5}, N. Dontschuk^{1,2,5}, A. Tsai¹, S. E. Lillie^{1,2}, C. T.-K. Lew^{1,2}, J. C. McCallum¹, B. C. Johnson^{1,2}, M. W. Doherty³, A. Stacey^{1,2,4}, L. C. L. Hollenberg^{1,2*} and J.-P. Tetienne^{1*}

Local variations in the charge distribution at semiconductor interfaces can lead to energy level band bending in the structure's band diagram. Measuring this band bending is important in semiconductor electronics and quantum technologies, but current methods are typically only surface sensitive and are unable to probe the extent of band bending at a depth within the semiconductor. Here, we show that nitrogen–vacancy centres in diamond can be used as in situ sensors to spatially map band bending in a semiconductor device. These nitrogen–vacancy quantum sensors probe the electric field associated with surface band bending, and we map the electric field at different depths under various surface terminations. Using a two-terminal device based on the conductive two-dimensional hole gas formed at a hydrogen-terminated diamond surface, we also observe an unexpected spatial modulation of the electric field, which is attributed to the interplay between charge injection and photoionization effects (from the laser used in the experiments). Our method offers a route to the three-dimensional mapping of band bending in diamond and other semiconductors that host suitable quantum sensors.

Band bending is a central concept in solid-state physics and is the result of local variations in charge distribution, especially near semiconductor interfaces and surfaces^{1–3}. Its precise determination is vital in a variety of contexts, including the development of optimized field-effect transistors (FETs)^{4–6} and the engineering of qubit devices with enhanced stability and coherence^{7–9}. However, existing measurement methods are surface sensitive^{1,10–12} and are unable to probe band bending at a depth from the surface. Measuring the precise spatial extent of band bending, which is linked to important quantities in FETs, such as the size of the depletion region, is therefore challenging since it depends not only on surface charge traps but also on bulk crystal defects and dopants.

Semiconductor-based quantum sensing technologies that can probe the behaviour of spins and charges have given rise to new opportunities in a range of areas across physics, materials science and biology^{13,14}. At present, most applications employ sensors that are external to the target sample^{15,16}. For instance, quantum sensors based on defects in diamond are routinely used to detect static or fluctuating magnetic signals from ferromagnets^{17,18} and from moving charges in conductive materials^{19,20}. However, in situ quantum sensors are also a valuable tool to study the sample itself and could enable three-dimensional (3D) mapping of internal quantities such as the magnetic field, electric field or temperature¹⁴. For semiconductor materials, these capabilities could, in particular, be used to gain information on the interaction between surface and bulk defects.

In this Article, we demonstrate a method based on in situ quantum sensors that can be used to spatially map the electric field near a semiconductor surface; this electric field (\mathcal{E}) is related to band bending via the standard relation

$$\mathcal{E}(\mathbf{r}) = \frac{1}{q} \nabla E_V(\mathbf{r}) \quad (1)$$

where $E_V(\mathbf{r})$ is the energy of electrons at the valence band maximum relative to the Fermi level (q is the electron charge). We use, specifically, the nitrogen–vacancy (NV) centre in diamond^{21,22}, a well-established atomic-sized quantum sensing system, which was recently shown to be a sensitive electrometer^{22,23}. NV centres can be positioned with a resolution of less than 1 nm in one dimension and 20 nm in the other two^{24–26}, which makes them ideal candidates for mapping built-in electric fields in three dimensions. As shown recently, it is possible to measure the electric field inside a diamond diode using single NV centres²⁷. In this Article, we engineer arrays of NV centres near the diamond surface to map the electric field associated with surface band bending. This concept can, in principle, be applied to other semiconductor systems that host quantum defects exhibiting the Stark effect, with promising candidates recently found in silicon²⁸ and silicon carbide^{29,30}.

Electric field near the diamond surface

The principle of the experiment is depicted in Fig. 1a. At the diamond surface, the bands bend to neutralize any surface charge due to ionized adsorbates or surface defect states, resulting in an electric field perpendicular to the surface with a magnitude $\mathcal{E}_z(z) = \frac{1}{q} \frac{dE_V}{dz}$. To probe this electric field, nitrogen ions were implanted to form NV centres³¹, following a spatial distribution that can be approximated as uniform over the depth range $d = 0–2\langle d \rangle$, where $\langle d \rangle$ is the (tunable) mean implantation depth³². To estimate \mathcal{E}_z , we first consider the case of commonly used oxygen-terminated diamond. It was recently found³³ that such samples typically host surface defects that introduce an acceptor level into the bandgap, with densities (D_{sd}) as high as 1 nm^{-2} . An example of a calculated electric field profile for this scenario (with parameters representative of our implanted samples) is plotted in Fig. 1b, predicting a maximum value at the surface of $\mathcal{E}_z \approx 1.6 \text{ MV cm}^{-1}$ and a characteristic decay length of approximately

¹School of Physics, University of Melbourne, Parkville, VIC, Australia. ²Centre for Quantum Computation and Communication Technology, School of Physics, University of Melbourne, Parkville, VIC, Australia. ³Laser Physics Centre, Research School of Physics and Engineering, Australian National University, Canberra, ACT, Australia. ⁴Melbourne Centre for Nanofabrication, Clayton, VIC, Australia. ⁵These authors contributed equally: D. A. Broadway, N. Dontschuk. *e-mail: lloydch@unimelb.edu.au; jtetienne@unimelb.edu.au

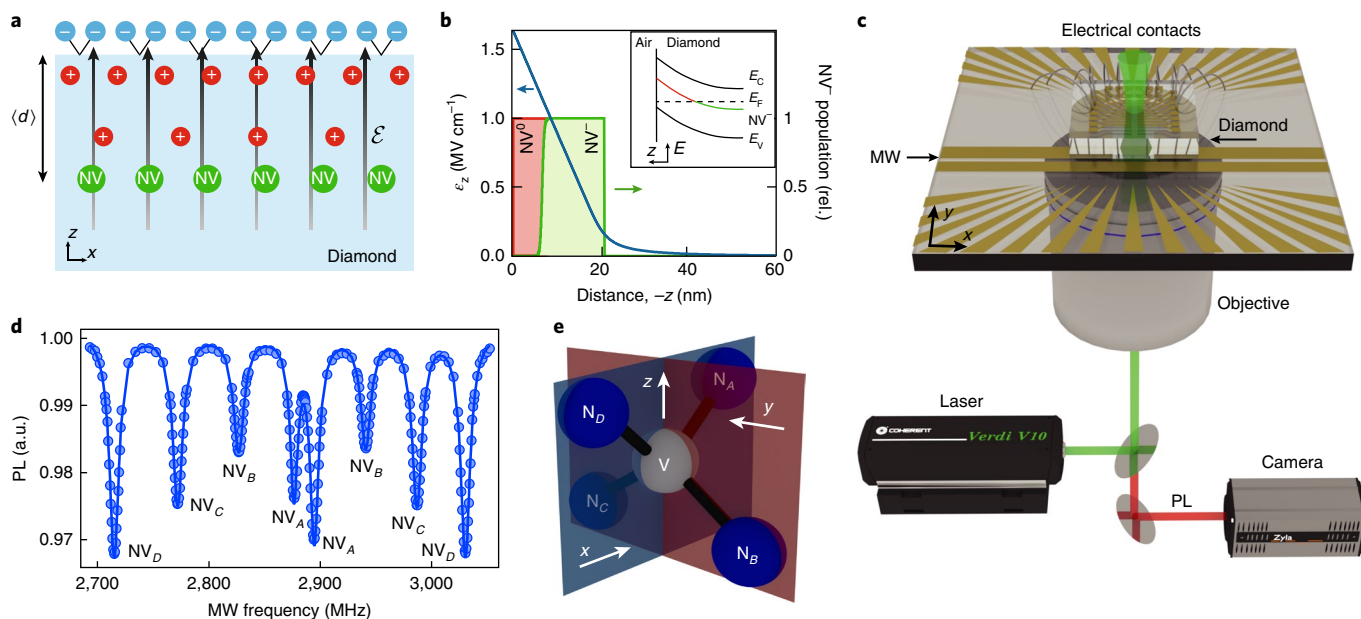


Fig. 1 | Mapping band bending with in situ quantum sensors. **a**, Principle of the experiment, where NV sensors (green dots) probe the electric field associated with surface band bending, here visualized as a distribution of space charge density. **b**, Calculated electric field profile for a typical (001)-oriented, O-terminated diamond surface, modelled as a layer of surface acceptor defects with a density of states centred at 1.5 eV above the valence band maximum³³ and a surface density $D_{sd} = 0.1 \text{ nm}^{-2}$ (see details in Supplementary Methods 2). The implanted substitutional nitrogen and NV defects are taken to be uniformly distributed over the range $d = 0\text{--}20 \text{ nm}$ (that is, $\langle d \rangle = 10 \text{ nm}$), with a total areal density of 0.1 nitrogen nm^{-2} . The green line is the NV^- population at equilibrium, and the green (red) shading represents the region where the NV^- (NV^0) charge state is dominant. Inset: corresponding band diagram near the surface, where E_C is the conduction band minimum, E_V the valence band maximum, E_F the Fermi level, and NV^- represents the charge transition level of the NV centre (that is, NV^- is the stable charge state when this level is below E_F). **c**, Diagram of the experimental set-up showing the diamond sample mounted on a glass slide patterned with gold to allow microwave (MW) injection and interfacing with electrical devices, illumination with a green laser and imaging of the NV red photoluminescence (PL) with a camera. **d**, Example ODMR spectrum recorded for an ensemble of near-surface NV centres in an O-terminated diamond under a magnetic field B_0 chosen to be perpendicular (within less than 3°) to a given NV family (here NV_A). Each resonance is labelled according to the corresponding NV orientation, defined in **e**. The solid line is a multiple-Lorentzian fit. **e**, The four possible tetrahedral orientations of the NV bond with respect to the sample reference frame xyz .

15 nm. We note that \mathcal{E}_z is positive (that is, the electric field points towards the surface), which corresponds to the bands bending upwards (inset in Fig. 1b), as expected from a positive space charge density near the surface (see Fig. 1a). As a consequence, only NVs deeper than a certain threshold (here approximately 7 nm for $\langle d \rangle = 10 \text{ nm}$) exist in the negatively charged state (NV^-) usable for sensing (Fig. 1b). The expectation value for an electric field measurement (that is, $\mathcal{E}_z(z)$ averaged over the NV^- distribution) is $\langle \mathcal{E}_z \rangle \approx 600 \text{ kV cm}^{-1}$, well in the range of sensitivity of the NV centre²². We note that the presence of the NV centres (and related implantation defects) affects the surface band bending, for instance a lower NV density would increase the spatial extent of the band bending. For truly non-invasive measurements of band bending, the NV density could be reduced to the single-site limit²⁷, although this approach is not compatible with real-space imaging.

We measured this electric field by optically detected magnetic resonance (ODMR) spectroscopy on the NV centres, using the experimental set-up depicted in Fig. 1c. An example ODMR spectrum obtained from a near-surface NV ensemble ($\langle d \rangle \approx 10 \text{ nm}$) is shown in Fig. 1d. A small magnetic field B_0 (of magnitude $B_0 \sim 6 \text{ mT}$) was applied to split the eight otherwise degenerate electron spin resonances corresponding to the four possible NV defect orientations relative to the diamond crystal (Fig. 1e), and carefully oriented so as to maximize the sensitivity to electric fields²² (see Supplementary Methods 1). The spectrum was fitted to extract the eight resonance frequencies, which are then compared to the standard NV spin Hamiltonian including the Zeeman and Stark effects^{22,34}, allowing us to infer the full vector magnetic and electric

fields simultaneously (except for an overall sign ambiguity, that is \mathcal{E} and $-\mathcal{E}$ yield the same ODMR spectrum). Importantly, we found that the measured frequencies could be satisfactorily fitted only when accounting for the Stark effect, providing clear evidence of the presence of a non-vanishing electric field (see fit error analysis in Supplementary Methods 1). For the data shown in Fig. 1d, we obtain $\langle \mathcal{E}_z \rangle = 372 \pm 5 \text{ kV cm}^{-1}$ (where we fixed $\mathcal{E}_x = \mathcal{E}_y = 0$ to reduce the uncertainty), reasonably close to our estimate.

To illustrate the 3D mapping capability, we formed NV centres at different depths in distinct diamonds and measured the electric field as explained above. We found that $\langle \mathcal{E}_z \rangle$ decreased from $432 \pm 10 \text{ kV cm}^{-1}$ at $\langle d \rangle \approx 7 \text{ nm}$ to $291 \pm 5 \text{ kV cm}^{-1}$ at $\langle d \rangle \approx 35 \text{ nm}$ (Fig. 2a), a trend relatively well captured by our model for D_{sd} in the range $0.06\text{--}1 \text{ nm}^{-2}$. Possible sources of discrepancy include: the influence of surface roughness, the presence of other types of surface or bulk defects than those considered in the model, and a depth profile different from that assumed.

Effect of the surface termination

We next studied the effect of surface termination on the electric field by forming a hydrogen-terminated (H) channel on an otherwise oxygen-terminated (O) diamond. An example of the resulting $\langle \mathcal{E}_z \rangle$ map is shown in Fig. 2b, revealing an increase from $372 \pm 5 \text{ kV cm}^{-1}$ in the O region to $410 \pm 5 \text{ kV cm}^{-1}$ in the H region. This is expected because H-terminated diamond is known to have a lower electron affinity, leading to efficient charge transfer from the diamond material onto acceptor species adsorbed on the surface in ambient air^{35,36}. This leads to increased band bending and hence the increased

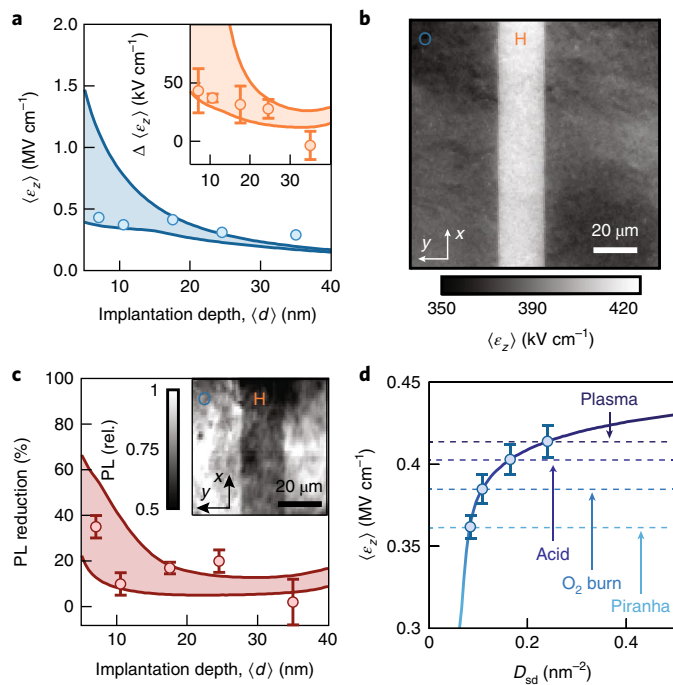


Fig. 2 | Electric field versus implantation depth and surface termination.

a, Electric field, $\langle \mathcal{E}_z \rangle$, as a function of the mean implantation depth, $\langle d \rangle$, for O-terminated diamond. Solid lines: result of the band bending model described in Fig. 1b with $D_{sd} = 0.06 \text{ nm}^{-2}$ (lower curve) and $D_{sd} = 1 \text{ nm}^{-2}$ (upper curve), with the shading representing intermediate values. Inset: difference $\Delta \langle \mathcal{E}_z \rangle = \langle \mathcal{E}_z \rangle_H - \langle \mathcal{E}_z \rangle_O$ between the electric field measured for H- and O-terminated diamond. Solid lines: model using a fixed density of charged surface adsorbates, $Q_{sa} = 0.07 \text{ nm}^{-2}$, and with $D_{sd} = 0.08 \text{ nm}^{-2}$ (upper curve) and $D_{sd} = 1 \text{ nm}^{-2}$ (lower curve). We note that the calculated $\langle \mathcal{E}_z \rangle$ takes into account the NV⁻/NV⁰ threshold distance, whose dependence on $\langle d \rangle$ and D_{sd} is plotted in Supplementary Fig. 15. **b**, $\langle \mathcal{E}_z \rangle$ map of an H-terminated channel on an O-terminated background ($\langle d \rangle \approx 10 \text{ nm}$). **c**, Photoluminescence (PL) reduction of the H region relative to the O region, as a function of $\langle d \rangle$. Solid lines: model using the same parameters as in inset of **a**. Inset: photoluminescence image of an H-terminated channel ($\langle d \rangle \approx 7 \text{ nm}$). **d**, $\langle \mathcal{E}_z \rangle$ versus D_{sd} calculated for $\langle d \rangle = 17 \text{ nm}$. The dashed lines and data points indicate the measured $\langle \mathcal{E}_z \rangle$ values for a comparable sample following various surface treatments, performed in the order: oxygen plasma (as used to form the O termination in **a-c**), acid cleaning, oxygen burning and piranha treatment (see details in Methods). Vertical error bars: $\pm \sigma$, where σ is the standard deviation.

electric field, beyond the threshold required to form a conductive two-dimensional hole gas (2DHG) near the surface³⁷, which is imaged in an electrical device described below. By fitting our model to the measured increase in $\langle \mathcal{E}_z \rangle$ caused by the H termination (inset in Fig. 2a), one can infer the density of charged surface adsorbates (acceptors), $Q_{sa} \approx 0.07 \text{ nm}^{-2}$, in rough agreement with the value derived from surface resistivity measurements (see Supplementary Methods 2). We stress that the two types of acceptor states introduced in the model (surface defects and surface adsorbates) are not equivalent because of their different energy levels—in particular, only the latter can give rise to a 2DHG. We also note that a resonance energy transfer from the NV centres to the conducting 2DHG may be present for the lowest implantation depths ($\langle d \rangle \lesssim 10 \text{ nm}$) effectively increasing the mean depth of the NV centres contributing to the signal, and as such it may provide an explanation for the fact that the measured increase in electric field by the H termination is slightly smaller than expected.

A consequence of the increased band bending is a decrease in the number of NV⁻ centres, which results in a decrease in the detected

photoluminescence, since the NVs closest to the surface become charge neutral³⁸. This is illustrated in Fig. 2c, which shows the photoluminescence reduction as a function of $\langle d \rangle$, with an example photoluminescence image of a H channel shown in the inset. This motivates the need to minimize band bending via surface engineering for quantum sensing applications, where the NV⁻ to surface distance is critical¹⁵. As a step towards this goal, we applied various surface treatments in an attempt to reduce the density of surface defects. Starting from a diamond initially O-terminated with an oxygen plasma as previously ($\langle \mathcal{E}_z \rangle \approx 414 \pm 10 \text{ kV cm}^{-1}$), we were able to reduce the electric field to approximately $362 \pm 6 \text{ kV cm}^{-1}$ through a combination of wet and dry treatments, which corresponds to a reduction of D_{sd} by nearly a factor of three according to our theory (Fig. 2d), and a reduction in the mean NV⁻ depth from approximately 23 nm to approximately 19 nm. These trends are broadly consistent with direct measurements of D_{sd} reported recently³³. We note that another avenue to reduce D_{sd} is by etching the diamond, as shown in Supplementary Data 3. These results illustrate the value of in situ electric field measurements, which may provide new insights into semiconductor surfaces and the effect of surface processing.

Electric field in an operating device

We now demonstrate mapping of the electric field in an electrical device consisting of a driven conductive 2DHG channel formed with an H-terminated diamond surface. Two-terminal devices were fabricated where TiC/Pt/Au contacts (source and drain) are connected by an H-terminated channel 100 μm in length and 20 μm in width (Fig. 3a,b). Unexpectedly, upon applying a voltage $V_{SD} = +100 \text{ V}$ an increase in $\langle \mathcal{E}_z \rangle$ was observed (by up to a factor of two) in a well-defined region of the channel extending over approximately 20 μm from the drain (Fig. 3c). Upon inversion of the voltage ($V_{SD} = -100 \text{ V}$), the feature moved to the other contact (Fig. 3d) to remain at the hole drain. In addition, we observed an influence of the lateral position of the laser illumination spot used for the measurements, which had a $1/e^2$ diameter of approximately 120 μm . In Fig. 3c,d, the laser spot was centred with respect to the device, as shown by the photoluminescence profile in Fig. 3e. When the centre of the laser spot was moved by 50 μm towards the right-hand contact (Fig. 3f–h, preserving sufficient illumination to allow ODMR measurement of the whole device), the region of increased electric field appeared to extend further away (approximately 40 μm) from the left-hand contact under positive voltage (Fig. 3f), and disappeared completely under negative voltage (Fig. 3g).

These observations are qualitatively interpreted as a combination of two competing effects, illustrated in Fig. 3i: the injection of electrons from the drain contact into charge traps in the diamond bulk, increasing the electric field seen by the NV centres, and laser-induced ionization of these charge traps, allowing the electrons to escape via the conduction band and returning the electric field to its zero-voltage value. These charge traps are probably the substitutional nitrogen impurities that are normally ionized by the band bending and become neutral near the drain contact when the voltage is applied. This interpretation is corroborated by the negative capacitance measured for these devices (see Supplementary Data 1). Line cuts taken at different voltages (Fig. 3j) reveal that the electric field decreases steadily from the contact (with a maximum value that increases monotonically with voltage, see Fig. 3k) before dropping off abruptly at a specific position independent of voltage (but dependent on laser position), even though the laser intensity increases approximately linearly with position (Fig. 3h). This suggests the existence of a strong nonlinearity in the ionization process as a function of laser intensity, possibly due to a change in the ionization energy of the charge traps caused by ionization of a second species of defects³⁹. These experiments illustrate how previously unobservable lateral changes in electric field, resulting from

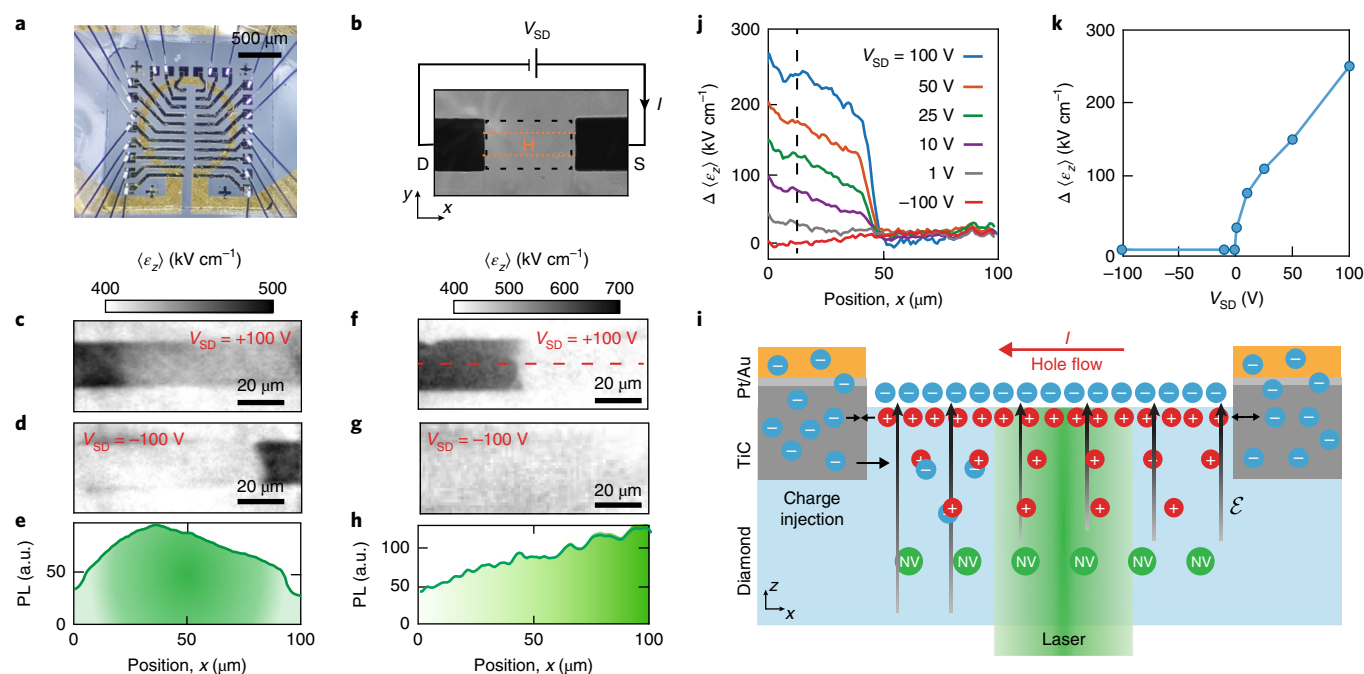


Fig. 3 | Electric field in a two-terminal device. **a**, Photograph of the diamond with the fabricated devices. **b**, Optical bright-field image of a device showing the TiC/Pt/Au contacts, defined as source (S) and drain (D). The optically-transparent 2DHG channel is indicated by orange dotted lines. The black dashed box defines the area imaged in **c-h**. **c,d**, $\langle \mathcal{E}_z \rangle$ map under an applied voltage $V_{SD} = +100$ V (**c**) and $V_{SD} = -100$ V (**d**), corresponding to a current through the channel of $I \approx \pm 400$ μ A. Note that this current generates a magnetic field that is completely separable from the electric field and can be imaged simultaneously (see Supplementary Methods 1). **e**, Line cut of the photoluminescence along the channel, indicative of the laser spot profile (indicated by the shading under the curve). **f-h**, Same as **c-e**, but with the laser spot offset by 50 μ m to the right. **i**, Diagram illustrating the different recombination and trapping processes for electrons under laser illumination and bias voltage. The TiC contact extends approximately 15 nm deep into the diamond (see Methods), with the NV centres implanted at a mean depth (d) \approx 17 nm. **j**, Line cuts of $\langle \mathcal{E}_z \rangle$ taken along the channel (see dashed line in **f**) for different voltages V_{SD} , with the laser spot centred as in **f-h**. **k**, Electric field measured at the position indicated by the black dashed line in **j**, plotted as a function of V_{SD} . In **j,k**, the zero-voltage value was subtracted to show only the increase caused by the applied voltage, $\Delta \langle \mathcal{E}_z \rangle$.

a complex contact/diamond junction, can be directly imaged and correlated with the electrical properties of the device (here a negative capacitance).

Conclusions

We have shown that NV centres in diamond can be used as in situ probes of the electric field associated with surface band bending. Furthermore, we applied this method to an electrical device based on the conductive H-terminated diamond surface, revealing an intriguing interplay between charge injection and photo-ionization effects.

Our method could be used to address a variety of questions in diamond electronics. It could, for example, be employed to examine hole transport behaviour in boron delta-doped diamond^{40,41}, which is of interest in the future development of high-power FETs. Probing the band bending in the vicinity of the delta layer could provide insight into why the high hole mobilities predicted for these structures (which also provide high carrier density) have not been achieved so far. Furthermore, our technique could be used to investigate H-terminated diamond FETs, which are also of potential value in the development of high-power and high-frequency electronics^{42,43}. With further improvements in the spatial resolution of the technique, it may for instance aid in understanding the origin of the suppression of weak anti-localization observed at low temperature^{44,45}, which is thought to be related to the spatial modulations of the confining potential (and thus band bending). More generally, systematic studies of the spatial distribution of band bending near the diamond surface could provide valuable knowledge on the surface and sub-surface defects present as a result of surface processing

and device fabrication, which may in turn guide the optimization of the hole mobility and hole carrier density in diamond-based FETs, which are the two key parameters governing device performance.

Surface properties are also crucial to semiconductor-based quantum technologies. They govern the charge stability of spin-defect qubits and may limit their quantum coherence⁷⁻⁹. Optimization of these metrics could certainly be facilitated by our technique. This includes the NV centre in diamond, whose charge state is intrinsically related to the surface band bending³³ and whose spin coherence is believed to be limited by surface defects⁴⁶⁻⁴⁸. It also includes other defects, such as the neutral silicon-vacancy defect in diamond, which require careful band engineering⁴⁹. Finally, another exciting prospect is to combine electric field mapping with other quantum sensing modalities such as current flow mapping^{20,50} and noise spectroscopy^{16,19}. This would allow charge transport and band bending to be simultaneously monitored in all-diamond FET devices or in hybrid structures based on 2D electronic systems such as graphene.

Methods

Diamond samples. The NV-diamond samples used in these experiments were made from 4 mm \times 4 mm \times 50 μ m electronic-grade ($[N] < 1$ ppb) single-crystal diamond plates with $\{110\}$ edges and a (001) top facet, purchased from Delaware Diamond Knives, subsequently laser cut into smaller 2 mm \times 2 mm \times 50 μ m plates and acid cleaned (15 min in a boiling mixture of sulphuric acid and sodium nitrate). Each plate was then implanted with $^{15}\text{N}^+$ ions (Innovion) at a given energy (ranging from 4 to 20 keV), a dose of 10^{13} ions cm^{-2} , and with a tilt angle of 7°. Parameters for each sample are given in Supplementary Table 1. Following implantation, the diamonds were annealed in a vacuum of approximately 10^{-5} torr to form the NV centres, using the following sequence³¹: 6 h at 400 °C, 2 h ramp to 800 °C, 6 h at 800 °C, 2 h ramp to 1,100 °C, 2 h at 1,100 °C, 2 h ramp to room temperature. To remove the graphitic layer formed during the annealing at the

elevated temperatures, the samples were acid cleaned (as before) before any further surface treatment or fabrication step.

Surface treatments. To form the H-terminated channels measured in Figs. 2b, c and 3, the diamond sample was first subject to a soft hydrogen plasma (7 min at 400 W, 10 torr) optimized to make the diamond surface conductive via hydrogenation while preserving the integrity of the NV centres³⁸. The channels were then protected by a photoresist mask and the sample subject to a soft oxygen plasma (5 min at 50 W, 14 MHz radiofrequency with a 0.7 torr O₂/Ar pressure) optimized to render the surface non-conductive via oxygen termination, while minimizing the amount of etching of the diamond. No topography step was observed in atomic force microscopy (AFM), indicating an etching by the oxygen plasma below our AFM resolution (that is, <0.5 nm).

In Fig. 2d, the effect of other variants of oxygen termination were investigated. Namely, starting with a diamond (sample #2) O-terminated via an oxygen plasma as described previously (labelled as 'Plasma' in Fig. 2d), we applied the following steps: acid cleaning (15 min in a boiling mixture of sulphuric acid and sodium nitrate); annealing at 500 °C in an oxygen-rich atmosphere similar to the process used in ref.⁵¹; cleaning in a piranha solution (mixture of 4 ml of sulphuric acid and 2 ml of hydrogen peroxide heated to 90 °C) for 10 min. The resulting surfaces are labelled in Fig. 2d as 'Acid', 'O₂ burn' and 'Piranha', respectively.

Device fabrication. The devices such as the one imaged in Fig. 3 were fabricated via the following steps (see a schematic in Supplementary Fig. 1). A stack of Ti/Pt/Au (thickness 10/10/70 nm) was evaporated onto the diamond (diamond #2) masked by a photoresist pattern. After lift-off of the photoresist leaving Ti/Pt/Au contacts, the sample was annealed at 600 °C for 20 min in hydrogen gas (10 torr). At such temperature, Ti atoms are able to diffuse into the diamond, and conversely carbon atoms are able to diffuse into the Ti layer, thus forming a TiC layer extending about 15 nm into the diamond. The thick Au layer serves as the primary contact material for electrical interfacing, while the Pt layer is introduced to act as a barrier preventing diffusion of Au and Ti atoms across the Ti/Au interface. The interest of such a process is to form a clean quasi-one-dimensional interface with the H-terminated channels subsequently fabricated. Together with the high expected work function of TiC (approximately 5 eV; ref.⁵²), this results in more consistent formation of Ohmic contacts than with conventional 2D interfaces of H-terminated diamond with Au (ref.⁵³) or Ti (ref.⁵⁴), for instance. After the TiC/Pt/Au contacts were formed, the H-terminated channels were made via the process outlined above (that is hydrogen plasma to H-terminate the bare diamond surface, photo-lithography to protect the channels, and oxygen plasma to O-terminate the unprotected diamond surface). Finally, large Cr/Au (10/70 nm) contact pads partially overlapped with the TiC/Pt/Au contacts were evaporated onto the device for physical wire bonding.

Imaging set-up. The NV imaging set-up is a custom-built wide-field fluorescence microscope similar to that used in refs.^{20,55}, with photographs shown in Supplementary Fig. 2. The diamonds were glued on a glass cover slip patterned with a microwave waveguide, connected to a printed circuit board (PCB) with silver epoxy. The diamond devices were electrically connected to the cover slip via wire bonding, and to the PCB board with silver epoxy. In Fig. 3, the voltage through the device under study was applied using a source-meter unit (Keithley SMU 2450) operated in constant voltage mode. All measurements were performed in an ambient environment at room temperature, under a bias magnetic field B₀ generated using a permanent magnet.

Optical excitation from a 532 nm Verdi laser was gated using an acousto-optic modulator (AA Opto-Electronic MQ180-A0,25-VIS), beam expanded (5×) and focused using a wide-field lens (*f* = 200 mm) to the back aperture of an oil immersion objective lens (Nikon CFI S Fluor 40×, NA = 1.3). The photoluminescence from the NV centres is separated from the excitation light with a dichroic mirror and filtered using a bandpass filter before being imaged using a tube lens (*f* = 300 mm) onto a sCMOS camera (Andor Zyla 5.5-W USB3). Microwave excitation was provided by a signal generator (Rohde & Schwarz SMBV100A) gated using the built-in IQ modulation and amplified (Mini-Circuits ZHL-16W-43+) before being sent to the PCB. A pulse pattern generator (SpinCore PulseBlasterESR-PRO 500 MHz) was used to gate the excitation laser and microwaves and to synchronize the image acquisition. For all measurements reported in the main text, the total continuous wave (CW) laser power at the sample was 300 mW (the effect of changing the laser power is investigated in Supplementary Data 2), which corresponds to a maximum power density of about 5 kW cm⁻² given the approximately 120 μm 1/e² beam diameter. The ODMR spectra of the NV layer were obtained by sweeping the microwave frequency while repeating the following sequence: 10 μs laser pulse, 1 μs wait time, 300 ns microwave pulse, with total acquisition times of several hours typically.

Data availability

The data underlying the present work are available upon request from the corresponding authors.

Received: 25 June 2018; Accepted: 14 August 2018;
Published online: 13 September 2018

References

- Zhang, Z. & Yates, J. T. Band bending in semiconductors: chemical and physical consequences at surfaces and interfaces. *Chem. Rev.* **112**, 5520–5551 (2012).
- Kotadiya, N. B. et al. Universal strategy for Ohmic hole injection into organic semiconductors with high ionization energies. *Nat. Mater.* **17**, 329–334 (2018).
- Simon, J., Protasenko, V., Lian, C., Xing, H. & Jena, D. Polarization-induced hole doping in wide-band-gap uniaxial semiconductor heterostructures. *Science* **327**, 60–64 (2010).
- Stathis, J. & Zafar, S. The negative bias temperature instability in MOS devices: a review. *Microelectron. Reliab.* **46**, 270–286 (2006).
- Zhang, P. et al. Electronic transport in nanometre-scale silicon-on-insulator membranes. *Nature* **439**, 703–706 (2006).
- Kaczer, B. et al. A brief overview of gate oxide defect properties and their relation to MOSFET instabilities and device and circuit time-dependent variability. *Microelectron. Reliab.* **81**, 186–194 (2018).
- Weber, J. R. et al. Quantum computing with defects. *Proc. Natl Acad. Sci. USA* **107**, 8513–8518 (2010).
- Kaviani, M. et al. Proper surface termination for luminescent near-surface NV centers in diamond. *Nano. Lett.* **14**, 4772–4777 (2014).
- Usman, M. et al. Spatial metrology of dopants in silicon with exact lattice site precision. *Nat. Nanotech.* **11**, 763–768 (2016).
- Kronik, L. & Shapira, Y. Surface photovoltage phenomena: theory, experiment, and applications. *Surf. Sci. Rep.* **37**, 1–206 (1999).
- Ishii, H. et al. Kelvin probe study of band bending at organic semiconductor/metal interfaces: examination of Fermi level alignment. *Phys. Stat. Sol. A* **201**, 1075–1094 (2004).
- Butler, C. J. et al. Mapping polarization induced surface band bending on the Rashba semiconductor BiTeI. *Nat. Commun.* **5**, 4066 (2014).
- Degen, C. L., Reinhard, F. & Cappellaro, P. Quantum sensing. *Rev. Mod. Phys.* **89**, 035002 (2017).
- Schirhagl, R., Chang, K., Loretz, M. & Degen, C. L. Nitrogen–vacancy centers in diamond: nanoscale sensors for physics and biology. *Annu. Rev. Phys. Chem.* **65**, 83–105 (2014).
- Rondin, L. et al. Magnetometry with nitrogen–vacancy defects in diamond. *Rep. Prog. Phys.* **77**, 056503 (2014).
- Casola, F., Van Der Sar, T. & Yacoby, A. Probing condensed matter physics with magnetometry based on nitrogen–vacancy centres in diamond. *Nat. Rev. Mater.* **3**, 17088 (2018).
- Tetienne, J.-P. et al. Nanoscale imaging and control of domain-wall hopping with a nitrogen–vacancy center microscope. *Science* **344**, 1366–1369 (2014).
- Du, C. et al. Control and local measurement of the spin chemical potential in a magnetic insulator. *Science* **357**, 195–198 (2017).
- Kolkowitz, S. et al. Probing Johnson noise and ballistic transport in normal metals with a single-spin qubit. *Science* **347**, 1129 (2015).
- Tetienne, J.-P. et al. Quantum imaging of current flow in graphene. *Sci. Adv.* **3**, e1602429 (2017).
- Doherty, M. W. et al. The nitrogen–vacancy colour centre in diamond. *Phys. Rep.* **528**, 1–45 (2013).
- Dolde, F. et al. Electric-field sensing using single diamond spins. *Nat. Phys.* **7**, 459–463 (2011).
- Dolde, F. et al. Nanoscale detection of a single fundamental charge in ambient conditions using the NV–center in diamond. *Phys. Rev. Lett.* **112**, 097603 (2014).
- Pezzagna, S. et al. Creation of colour centres in diamond by collimated ion implantation through nano-channels in mica. *Phys. Stat. Sol. A* **208**, 2017–2022 (2011).
- Ohno, K. et al. Engineering shallow spins in diamond with nitrogen delta-doping. *Appl. Phys. Lett.* **101**, 082413 (2012).
- Lesik, M. et al. Production of bulk NV centre arrays by shallow implantation and diamond CVD overgrowth. *Phys. Stat. Sol. A* **213**, 2594–2600 (2016).
- Iwasaki, T. et al. Direct nanoscale sensing of the internal electric field in operating semiconductor devices using single electron spins. *ACS Nano* **11**, 1238–1245 (2017).
- Zhang, Q. et al. Single rare-earth ions as atomic-scale probes in ultra-scaled transistors. Preprint at <https://arXiv.org/abs/1803.01573> (2018).
- Falk, A. L. et al. Electrically and mechanically tunable electron spins in silicon carbide color centers. *Phys. Rev. Lett.* **112**, 187601 (2014).
- Wolfowicz, G., Whiteley, S. J. & Awschalom, D. D. Electrometry by optical charge conversion of deep defects in 4H-SiC. Preprint at <https://arXiv.org/abs/1803.05956> (2018).
- Tetienne, J.-P. et al. Spin properties of dense near-surface ensembles of nitrogen–vacancy centers in diamond. *Phys. Rev. B* **97**, 085402 (2018).
- Lehtinen, O. et al. Molecular dynamics simulations of shallow nitrogen and silicon implantation into diamond. *Phys. Rev. B* **93**, 35202 (2016).
- Stacey, A. et al. Evidence for primal sp² defects at the diamond surface: candidates for electron trapping and noise sources. Preprint at <https://arXiv.org/abs/1807.02946> (2018).

34. Doherty, M. W. et al. Theory of the ground-state spin of the NV⁻ center in diamond. *Phys. Rev. B* **85**, 205203 (2012).
35. Strobel, P., Riedel, M., Ristein, J. & Ley, L. Surface transfer doping of diamond. *Nature* **430**, 439 (2004).
36. Maier, F., Riedel, M., Mantel, B., Ristein, J. & Ley, L. Origin of surface conductivity in diamond. *Phys. Rev. Lett.* **85**, 3472–3475 (2000).
37. Pakes, C. I., Garrido, J. A. & Kawarada, H. Diamond surface conductivity: Properties, devices, and sensors. *MRS. Bull.* **39**, 542–548 (2014).
38. Hauf, M. V. et al. Chemical control of the charge state of nitrogen–vacancy centers in diamond. *Phys. Rev. B* **83**, 081304 (2011).
39. Dhomkar, S., Jayakumar, H., Zangara, P. R. & Meriles, C. A. Charge dynamics in near-surface, variable-density ensembles of nitrogen–vacancy centers in diamond. *Nano. Lett.* **18**, 4046–4052 (2018).
40. Chicot, G. et al. Hole transport in boron delta-doped diamond structures. *Appl. Phys. Lett.* **101**, 162101 (2012).
41. Scharpf, J. et al. Transport behaviour of boron delta-doped diamond. *Phys. Stat. Sol. A* **210**, 2028–2034 (2013).
42. Kawarada, H. High-current metal oxide semiconductor field-effect transistors on H-terminated diamond surfaces and their high-frequency operation. *Jpn. J. Appl. Phys.* **51**, 090111 (2012).
43. Kasu, M. Diamond field-effect transistors for RF power electronics: Novel NO₂ hole doping and low-temperature deposited Al₂O₃ passivation. *Jpn. J. Appl. Phys.* **56**, 01AA01 (2017).
44. Edmonds, M. T. et al. Spin–orbit interaction in a two-dimensional hole gas at the surface of hydrogenated diamond. *Nano. Lett.* **15**, 16–20 (2015).
45. Akhgar, G. et al. G-factor and well width variations for the two-dimensional hole gas in surface conducting diamond. *Appl. Phys. Lett.* **112**, 042102 (2018).
46. Myers, B. A. et al. Probing surface noise with depth-calibrated spins in diamond. *Phys. Rev. Lett.* **113**, 027602 (2014).
47. Roskopf, T. et al. Investigation of surface magnetic noise by shallow spins in diamond. *Phys. Rev. Lett.* **112**, 147602 (2014).
48. Romach, Y. et al. Spectroscopy of surface-induced noise using shallow spins in diamond. *Phys. Rev. Lett.* **114**, 017601 (2015).
49. Rose, B. C. et al. Observation of an environmentally insensitive solid-state spin defect in diamond. *Science* **361**, 60–63 (2018).
50. Chang, K., Eichler, A., Rhensius, J., Lorenzelli, L. & Degen, C. L. Nanoscale imaging of current density with a single-spin magnetometer. *Nano. Lett.* **17**, 2367–2373 (2017).
51. Lovchinsky, I. et al. Nuclear magnetic resonance detection and spectroscopy of single proteins using quantum logic. *Science* **351**, 836–841 (2016).
52. Kim, C. K. et al. Temperature control for the gate workfunction engineering of TiC film by atomic layer deposition. *Solid. State. Electron.* **114**, 90–93 (2015).
53. Hauf, M. V. et al. Low dimensionality of the surface conductivity of diamond. *Phys. Rev. B* **89**, 115426 (2014).
54. Akhgar, G. et al. Strong and tunable spin–orbit coupling in a two-dimensional hole gas in ionic-liquid gated diamond devices. *Nano. Lett.* **16**, 3768–3773 (2016).
55. Simpson, D. A. et al. Magneto-optical imaging of thin magnetic films using spins in diamond. *Sci. Rep.* **6**, 22797 (2016).

Acknowledgements

We thank M. Barson, D. Simpson and L. Hall for useful discussions. We acknowledge support from the Australian Research Council (grants CE110001027, DE170100129, FL130100119, DP170102735). J.-PT acknowledges support from the University of Melbourne through an Early Career Researcher Grant. D.A.B, A.T, S.E.L and C.T.-K.L are supported by an Australian Government Research Training Program Scholarship. This work was performed in part at the Melbourne Centre for Nanofabrication (MCN) in the Victorian Node of the Australian National Fabrication Facility (ANFF).

Author contributions

NV measurements and analysis were performed by D.A.B and J.-PT, with inputs from M.W.D. The devices were fabricated by N.D and D.A.B, H-terminated by A.T and A.S, and electrically characterized by C.T.-K.L and B.C.J. The band bending model was developed by N.D with inputs from D.A.B, J.-PT, A.S and L.C.L.H. All authors contributed to interpreting the data and writing the manuscript.

Competing interests

The authors declare no competing interests.

Additional information

Supplementary information is available for this paper at <https://doi.org/10.1038/s41928-018-0130-0>.

Reprints and permissions information is available at www.nature.com/reprints.

Correspondence and requests for materials should be addressed to L.C.L.H. or J.-PT.

Publisher's note: Springer Nature remains neutral with regard to jurisdictional claims in published maps and institutional affiliations.